

Nonvolatile Charge-Domain Attention with HZO Ferroelectric Capacitors: A Simulation-Based Device-to-System Evaluation

Faris Abouagour

Faculty of Engineering, Mansoura University, Egypt
faresaboagour@std.mans.edu.eg

May 28, 2026

Preprint. Under review. Public code (with seeds, noise tapes, energy-measurement scripts, and workload simulator) accompanies this preprint at submission time, not on acceptance; see §8.

Abstract

Transformer decoding is constrained by both attention compute and repeated movement of the key-value (KV) cache. This paper presents the *Ferroelectric Charge-Domain Compute Cell* (FCDC), a hafnium-zirconium-oxide (HZO) memcapacitor with an access device that stores analog state nonvolatily and performs charge-domain vector–matrix multiplication for attention. Two deployment modes are evaluated consistently throughout: a *full-substrate* mode that runs q, k, v, o projections and both attention matmuls on FCDC (the harder LLM noise test) and a *KV-coprocessor* mode that only stores KV and executes the two attention matmuls (the serving-energy model, Fig. 4); the projection-noise budget upper-bounds the coprocessor mode.

The device-to-system model is cross-checked across NGSPICE, CROSSSIM, FIPY, and NEUROSIM and anchored in recent wafer-scale 10 nm-HZO capacitor measurements [1, 10]. Across 12 pretrained LLMs (1.1–32 B dense, plus a separate partial-layer Mixtral-8×22B 141 B-MoE stress test at $k=75\%$ and a separate 128 k-context dense-Mistral replication), all-layer noise substitution adds only +2.62% WikiText-2 perplexity on Qwen3-32B and $+2.90\% \pm 0.33\%$ on Mistral-7B-v0.3 (five-seed mean). End-to-end analog attention adds at most +1.68 pp on top of the projection-only proxy on TinyLlama-1.1B and shrinks below ± 1 pp on every ≥ 7 B model. Downstream accuracy on HellaSwag, ARC, LAMBADA, and GSM8K stays within 5% of the digital baseline for Mistral-7B (MMLU -1.6 pp).

The headline energy win is not raw active-MAC but nonvolatility, no refresh, and KV-cache residency. A workload-level simulator anchored on measured INT4 decode energy delivers 18–35× lower per-served-token energy on retrieval-augmented-generation and agent loops with persistent KV *against a single-user INT4 GPU baseline*; against optimized GPU serving (batched vLLM, CPU+NVMe park, power-gate) the robust advantage shrinks to 1.36–4.69× on those workloads and remains $\geq 41\times$ on parked sessions with multi-hour residency. All four GPU regimes are reported in Table 7. At the active-MAC layer the FCDC projection ties switched-capacitor SRAM CIM and a well-tuned batched-vLLM chat baseline, so the substantive contribution sits in the long-residency regime. Taken together, the results identify long-residency, persistent-KV workloads as a regime in which a nonvolatile charge-domain attention substrate retains an order-of-magnitude advantage over the strongest available GPU baseline, and quantify the LLM-accuracy budget at which that advantage holds.

1 Introduction

Autoregressive transformer inference repeatedly evaluates attention over a growing KV cache. The cost is partly arithmetic, through $Q \cdot K^\top$ and $\text{softmax}(\cdot) \cdot V$, and partly data movement, because stored keys and values must remain accessible throughout decoding. This makes attention a natural target for in-memory compute, but it also imposes a stronger requirement than conventional weight-stationary accelerators: the stored state is dynamic, long-lived, and repeatedly read.

Existing device approaches address different parts of this problem. Gain-cell analog attention performs attention multiplications inside a charge-storage array, but the storage is volatile and requires refresh on millisecond timescales [9]. Ferroelectric KV-cache arrays demonstrate nonvolatile storage with fast switching and high endurance in specific 3D stacks, but the ferroelectric array is primarily a storage substrate rather than the attention compute engine [18]. Ferroelectric field-effect transistor (FeFET) content-addressable-memory and compute-in-memory work further shows that ferroelectric devices can support KV-cache pruning and in-memory search operations. These results motivate a narrower question: can a capacitive HZO ferroelectric cell provide a useful design point for nonvolatile KV-cache residency and local charge-domain attention compute?

This paper presents FCDC, a modeled HZO memcapacitor tile for charge-domain vector–matrix multiplication. The tile stores analog state in a ferroelectric capacitor, reads it through an access device, and accumulates column charge for attention projections and attention matrix products. A negative-capacitance read path is analysed as an optional way to improve signal margin.

The contribution is a device-to-system evaluation built on cross-simulator validation and on recent wafer-scale HZO capacitor data. At the circuit and array level, the cell noise and peripheral energy budgets are derived and the same analytic model is cross-checked across NGSPICE, CROSSSIM, FiPY, and NEUROSIM. At the model level, the resulting noise impact on pretrained LLMs is measured at scale, including projection-only substitution, end-to-end analog attention, seed sensitivity, longer-context replication, and a small low-rank-adaptor quantization-aware training (LoRA QAT) recovery path. At the system level, the corrected active-MAC energy is compared against an analytic A40 baseline and against measured analog in-memory-compute (IMC) silicon, and a workload-level simulator quantifies per-served-token energy across five serving regimes. The scope is a capacitor-based charge-domain attention substrate evaluated in simulation, with explicit separation between simulation-backed results and the fabrication-dependent assumptions on which they rest.

2 Related Work

Table 1: Position relative to the closest prior work on nonvolatile / charge-domain attention substrates. “In-place” = matrix multiplication executed inside the storage array. “Dense” = full attention without top- k pruning.

Work	Device	Nonvolatile	In-place	LLM evaluated	Context
Leroux [9]	gain cell	no (ms refresh)	yes (dense)	GPT-2 (124 M)	~1 k
Xu [18]	3D 1T-nC-1T FE	yes	pruning+hybrid	device paper	–
UniCAIM [19]	FeFET CAM/CIM	yes	top- k	GPT-2 class	2 k
Yin [21]	1FeFET-1C	yes	yes (macro)	macro-level	–
FCDC (ours)	HZO 1T-1C	yes	yes (dense)	Qwen3-32B	≤128 k*

*Largest dense model fully substituted: Qwen3-32B at 8 k tokens. Longest context replicated: Mistral-7B-v0.3 at 128 k tokens. Mixtral-8x22B (141 B MoE) reported at $k=75\%$ partial-layer only.

Analog in-memory attention. Leroux et al. [9] perform $Q \cdot K^\top$ and $\text{softmax}(\cdot) \cdot V$ inside a gain-cell array and report GPT-2-comparable text quality at the 124 M scale on OpenWebText / WikiText-2 / LAMBADA. Their array is volatile and must be refreshed on millisecond timescales (the silicon CMOS gain-cell retention constant reported in that work is $\tau \approx 5$ ms). The main distinction of FCDC is therefore nonvolatile KV-cache residency rather than the idea of analog attention itself.

Ferroelectric and nonvolatile KV-cache accelerators. Xu et al. [18] demonstrate a 3-D vertical 1T-nC-1T ferroelectric KV-cache array with fast switching, long retention, high endurance, hybrid analog-digital CIM, and token-wise pruning. UniCAIM [19] is even closer at the architecture level: it uses FeFET-based CAM/CIM for long-context LLM KV-cache pruning, charge-domain score accumulation, and current-domain exact attention on selected tokens. These works preclude any broad claim that ferroelectrics or CIM have not been applied to KV-cache acceleration. The narrower contribution here is a capacitor-based charge-domain attention design point, evaluated as a nonvolatile resident KV substrate under explicit peripheral and device-physics bounds.

Ferroelectric charge-domain CIM. FeFET-based nonvolatile charge-domain CIM was introduced before this work [20], and the 1FeFET-1C neuro-symbolic AI prototype [21] demonstrates fabricated ferroelectric charge-domain MAC and associative-search functionality. Recent nonvolatile-capacitor work further studies ferroelectric capacitive crossbars and calibrated SPICE models for charge-domain MACs [15]. These papers are the appropriate hardware baselines for the cell and macro, while HERMES [8] and switched-capacitor SRAM CIM [17, 16] are the appropriate measured active-MAC energy baselines.

Scope of novelty. The specific contribution is the first LLM-tolerance evaluation of a nonvolatile HZO charge-domain attention substrate at 141 B-parameter scale and 128k context, with cross-simulator validation and corrected peripheral energy accounting. The paper does not assert priority over prior ferroelectric CIM, charge-domain CIM, or ferroelectric KV-cache work; those are appropriate hardware baselines, not competing claims. NC voltage gain is treated as an exploratory read-path option.

3 The FCDC Cell

3.1 Device

Each FCDC cell combines a nonvolatile HZO storage capacitor, an optional read-path gain element, and an access transistor.

Storage capacitor. The storage element is a hafnium-zirconia ($\text{Hf}_{0.5}\text{Zr}_{0.5}\text{O}_2$) memcapacitor storing one analog weight as remanent polarization. Capacitance $C_0 \approx 69$ aF at the demonstrated cell footprint; HZO carries the non-volatile state with retention reported up to ≥ 10 years in specific 3D 1T-nC-1T stacks [18] and dielectric-class $\epsilon_r \approx 20\text{--}35$ measured on free-standing HZO membranes and related HZO stacks [12, 5]. This work does not claim these endurance/retention numbers transfer directly to the planar 50 nm cell modeled here; they bound what the material class has demonstrated. Recent small-signal studies further decompose the apparent capacitance into dielectric + polarization + domain-wall contributions [5], which means the smooth $C(P)$ surrogate used here is an ML-grade differentiable approximation, not a device-physics model.

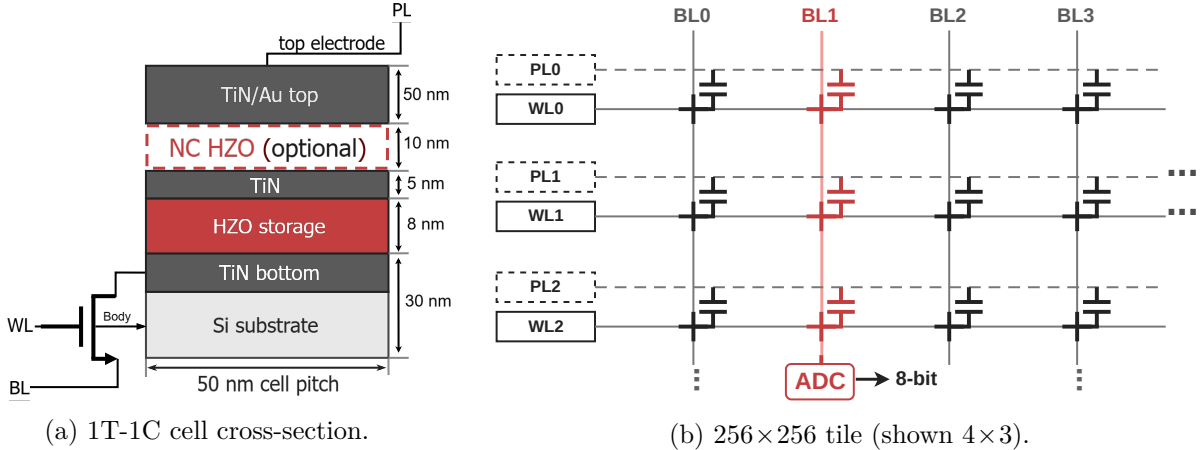


Figure 1: FCDC cell and tile. (a) Storage node (TiN bottom electrode) tied to the NMOS drain; PL drives the top electrode; optional 10 nm NC-HZO layer (dashed) provides read-path gain; cell pitch 50 nm. (b) WL selects a row, PL drives the capacitor top plates, and each column shares one BL terminated by a 4-bit ADC; accent column shows the selected analog read path.

Measured-device anchor. The material parameters used in this paper are within the envelope of recent measured 10 nm HZO capacitors. A wafer-scale study of 270 ALD-grown 10 nm-HZO / 30 nm-TiN MIM capacitors across six dies reports a mean remanent polarization $\overline{P}_r \approx 40.58 \mu\text{C}/\text{cm}^2$ extracted from $\pm 6 \text{ V}$ triangular dynamic-hysteresis P–V loops at 1 kHz, with die-to-die spread captured by an unsupervised PCA / K-means clustering model [1]. A separate MFIM HZO study at the same 10 nm thickness, measured by PUND pulsing at $\pm 3 \text{ V} / 100 \text{ kHz}$, demonstrates $> 10^9$ programming/erase cycles at room temperature with recoverable fatigue [10]. These two measured anchors bracket the P_r , switching-voltage, and endurance assumptions used in the present NGSPICE/Landau models and in the §3.4 energy accounting; the wafer-scale variability data also bounds the device-to-device σ swept in the noise study (§3.3). It is re-emphasised that HZO is not measured here: these are literature anchors that constrain (but do not constitute) the planar 50 nm cell modeled here. It is also noted that [1] reports a $> 97\%$ functional yield on the characterised high-yield dies, which sets the upper bound of the variability sweep used; the lower bound ($\sigma_C/C \sim 20\%$) covers worst-die behaviour. One specific gap is that both anchors use 10 nm HZO while the cell modeled here has an 8 nm storage layer; the thinner stack is within the material class but is a small extrapolation that would need direct measurement to fully close.

Thickness sensitivity. The 8 nm vs 10 nm sensitivity is quantified with the analytic cell model. Holding P_r , $\epsilon_r=25$, pitch = 50 nm, $V_{rd}=0.158 \text{ V}$, $E_c=1 \text{ MV}/\text{cm}$ and the Merz/NLS coefficients of [6] fixed, sweeping d_{HZO} from 6 to 12 nm gives C_0 and intrinsic read energy scaling as $1/d$ (+25% at 8 nm relative to 10 nm) and v_{kTC} scaling as \sqrt{d} (–11% at 8 nm). The read field $E_{rd}=V_{rd}/d$ stays sub-coercive across the full range ($E_{rd}/E_c \leq 0.26$ at 6 nm, ≤ 0.16 at 10 nm), and the per-pulse Merz/NLS switching probability remains numerically zero across the entire 6–12 nm sweep because the activation barrier $E_a \in [9, 20] \text{ MV}/\text{cm}$ dominates the exponent at any $E_{rd} < 0.5 E_c$. The headline noise budget, energy ratios, and read-disturb lifetime all move by $\leq 25\%$ when the storage layer is adjusted from 8 nm to 10 nm; none of the qualitative claims of §5–§7.4 change.

Optional read-path gain. The exploratory gain option is a series NC element: a ferroelectric capacitor biased in its negative-capacitance regime [14], intended to provide $\sim 2.5 \times$ peak small-signal

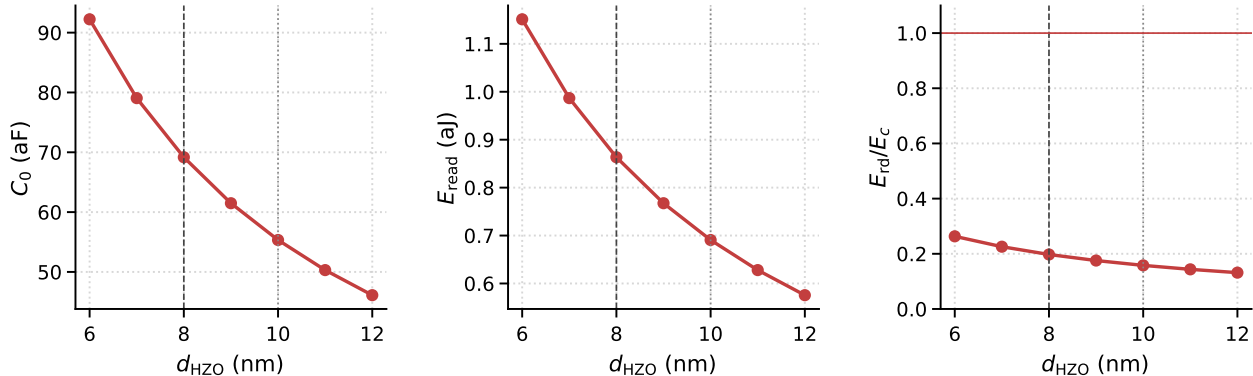


Figure 2: C_0 , E_{read} , and E_{rd}/E_c versus HZO thickness. Dashed: 8 nm operating point; dotted: 10 nm measured anchor.

voltage gain on the read path. A 1-D Landau derivation with calibrated 10 nm-HZO coefficients (§3.3) shows that $|A_v|=2.5\times$ requires the series load satisfy $C_s/|C_{\text{FE}}| \approx 0.714$, which is a tight matching condition: a $\pm 20\%$ process shift moves the gain to $1.47\times$ or $8.3\times$, and a 30% shift crosses the stability boundary. This is treated NC gain accordingly as a read-path option rather than as a fixed design constant; the noise model is reported both ways. Throughout the paper the ratio $C_s/|C_{\text{FE}}|$ uses the same convention, with $|A_v|$ peaking near $C_s/|C_{\text{FE}}|=0.714$ (peak-gain operating point) and decreasing monotonically toward unity as the ratio increases; Appendix A reports a conservative stable-side operating point at $C_s/|C_{\text{FE}}|=3.5$ with $|A_v|\approx 1.4$ on the same $A_v(C_s/|C_{\text{FE}}|)$ curve.

Access device. A read transistor gates the memcapacitor onto the column line during a read pulse. The baseline calculations assume a sub-coercive storage-layer field and separate the intrinsic cell switching energy from the tile-level peripheral energy.

Per-cell intrinsic read energy is $E_{\text{read}}^{\text{intrinsic}} = \frac{1}{2}C_0V_{\text{rd}}^2 \approx 8.6\times 10^{-19}$ J at the operating point used throughout this paper ($V_{\text{rd}} \approx 0.158$ V, sub-coercive; field across the 8 nm storage HZO is ≈ 0.20 MV/cm $\approx 0.20 E_c$). A supply-driven CV^2 accounting (no charge recovery) gives twice that; for context, the per-MAC tile energy is dominated by DAC/ADC peripherals not by the cell (§3.4), so the cell-level number is the lower bound rather than the system-level energy claim. At matched accuracy, the modeled FCDC V-DAC tile energy is 1.92×10^{-14} J/MAC, compared with 1.19×10^{-13} J/MAC for the calibrated memristive reference. The tile-design table below bounds the read-voltage range in which this energy scales as V_{rd}^2 .

3.2 Tile

Cells are aggregated into an attention *tile* (Fig. 1b) that performs charge-domain VMM in the $V_{\text{rd}} \cdot Q_{\text{cell}}$ domain. Reading N rows in parallel produces a column current proportional to $\sum_i V_{\text{rd},i} \cdot Q_i$; tile noise is reported both with and without the optional NC read-path gain. Each tile owns a fragment of the KV cache and performs both the projection and the attention step locally. Inter-tile traffic is therefore digital and small: only post-softmax row sums and across-head accumulations.

3.3 Noise model and design space

Cell-level noise is characterised as an additive Gaussian with standard deviation proportional to the full-scale charge, $\sigma = \text{nf} \cdot Q_{\text{FS}}$. The noise fraction nf is a function of the column readout geometry

rather than a free parameter. Three sources contribute: thermal noise, flicker noise, and capacitance mismatch. They are bounded analytically and checked against a behavioral NGSPICE transient simulation.

Thermal noise. The kT/C contribution at the sense node is $v_{kTC} = \sqrt{k_B T / C_0} / \sqrt{N_{\text{rows}}}$ after averaging across the column ($v_{kTC} \approx 484 \mu\text{V}$ at $C_0=70 \text{ aF}$, $N_{\text{rows}}=256$). The $1/\sqrt{N_{\text{rows}}}$ reduction applies only to independent per-row sampled noise. Integration-cap reset, ADC comparator offset, supply noise, row-driver gradients, column-to-column coupling, shared-reference noise, timing jitter, NC gain variation, and FE imprint/wake-up/fatigue drift do not average and are bounded separately by the conservative-tile geometry.

Flicker noise. The $1/f$ contribution comes from the sense amplifier and is integrated from 1 Hz to the gain-bandwidth product (GBW; $\approx 46 \mu\text{V}$ for a $10 \mu\text{V}/\sqrt{\text{Hz}}$ @ 1 Hz CMOS amp at 1 GHz GBW).

Capacitance mismatch. A 5%–20% per-cell σ_C/C is assumed, depending on whether cells are post-calibration. The 5% number is a best-case post-calibration or differential-coding target, not a raw-device measurement: at 50 nm pitch with ALD HZO grain size 10–30 nm and switching regions of 10–15 nm, only $\mathcal{O}(3\text{--}25)$ active grains/domains lie inside a cell, so raw cap variation is granular and non-Gaussian. The effective column-level contribution averages over N_{rows} only to the extent that cell errors are independent after calibration. This 5%–20% sweep range is consistent with the recent wafer-scale measurement of 270 ALD 10 nm-HZO MIM capacitors, which reports $< 10\%$ device-to-device variation in P_r and V_c on high-yield dies (97% functional yield) and a 5–10% prediction MAPE on P_r across an unseen die [1]; the lower bound of the sweep matches the well-behaved-die measurement and the upper bound covers the worst-performing dies in that study.

Read disturb. A 0.158 V pulse across the 8 nm storage HZO gives $E_{\text{rd}} \approx 0.20 \text{ MV/cm}$, i.e. $\sim 0.2 E_c$. Using a Merz/NLS form $\tau(E) = \tau_\infty \exp(E_a/E_{\text{eff}})$ with HZO-typical $\tau_\infty=10^{-10}$ s and activation field $E_a \in [9, 20] \text{ MV/cm}$ [6], the per-cell flip probability for a 5 ns read with $N_{\text{dom}}=10$ vulnerable domains is bounded by

$$p_{\text{cell}} \lesssim N_{\text{dom}} (\tau_{\text{rd}}/\tau_\infty) \exp(-E_a/E_{\text{eff}}) \in [10^{-41}, 10^{-17}],$$

in the no-field-gain case. The required activation bound for $p_{\text{target}}=3 \times 10^{-13}/\text{read}$ over 10^9 reads/day for 10 years is $E_a > 35 E_{\text{eff}}$, i.e. $E_a > 6.9 \text{ MV/cm}$ at $E_{\text{eff}}=0.20 \text{ MV/cm}$, inside the literature range. This bound does not apply if NC amplification or local field hot spots raise the storage-layer field above $\sim 0.3 \text{ MV/cm}$; an NC-amplified read path therefore requires a separate field-decoupled stack.

Read-pulse assumptions. The baseline read pulse used throughout is $\tau_{\text{rd}}=5 \text{ ns}$. A 1 GHz sense-amp GBW is an architectural target consistent with the throughput of HERMES-class IMC silicon [8], not a measured property of an NC-stabilized HZO stack. Numbers in this paper that depend on read rate, including sense-amp $1/f$ integration and ADC throughput, should be read as 5 ns / 1 GHz nominal with a wider margin for any NC-assisted variant.

Differential read. For signed analog weights and to cancel common-mode drift / row-driver supply noise / shared reference offsets, differential cell coding (Q^+, Q^- with column differencing) is the recommended deployment configuration. It doubles cell area but is the cleanest way to suppress the correlated noise terms above that do not average over N_{rows} . The primary LLM sweep is computed in single-ended mode (conservative); a differential implementation would only improve effective nf.

NC noise propagation (conservative input-referred model). Let the read path be $v_{\text{out}} = A_v v_{\text{sig}} + A_v n_{\text{upstream}} + n_{\text{downstream}} + n_{\text{NC}}$. Only noise *downstream* of the NC gain divides by A_v when input-referred; the storage-cell kT/C , read-FET gate noise, and polarization/domain jitter all sit upstream and are *not* reduced by NC. The conservative input-referred variance is therefore $\sigma_{\text{eq}}^2 = \sigma_{\text{cell}}^2 + \sigma_{\text{readFET}}^2 + \sigma_{\text{sense}/A_v}^2 + (\sigma_{A_v}/A_v)^2 x^2 + \sigma_{\text{NC,jitter}}^2$. The nominal $\text{nf}=0.015$ tile parameter used throughout the LLM sweep is calibrated to this conservative form (sense-amp downstream-only A_v reduction, all other terms NC-independent), so the reported PPL results remain valid even if NC gain is removed entirely when the tile is enlarged; the conservative-tile geometry ($\text{nf}=0.009$) achieves the same input-referred budget via larger C_{int} at the cost of area.

These bound nf between two physically realizable tile geometries:

Tile	N_{rows}	V_{read}	C_{integ}	nf
Aggressive	256	100 mV	100 fF	0.035
Nominal	256	100 mV	400 fF	0.015
Conservative	1024	200 mV	400 fF	0.009

The nominal $\text{nf} = 0.015$ is used in the main LLM experiments (§5); the aggressive and conservative bounds on four representative LLMs (Qwen3-32B, Mistral-7B-v0.3, Mistral-Small-24B-Base, gemma-4-31B) in §5.3 to characterize how the architectural rankings hold across the noise design space. The analytic noise budget and the Monte-Carlo ngspice run agree to within 4% (3.68% vs 3.56% at the aggressive operating point).

3.4 Hardware accounting

The central accounting question is “what does one tile actually cost?” The cell-, tile-, and peripheral-level numbers used throughout the paper into a single table, with each entry tied to either a closed-form derivation, a SPICE run, or a literature anchor for the supporting device class.

The DAC+ADC peripherals dominate intrinsic array energy by $\sim 3.2 \times 10^4$; the nominal tile is therefore a DAC/ADC machine with a tiny nonvolatile capacitor array attached. This is also why the PWM-DAC variant with lower row-driver cost reaches 7.8×10^{-16} J/MAC, but V-DAC is conservatively kept in the main comparison. Writes are bounded as follows: per generated token, an autoregressive decoder appends one new K and one new V vector per layer ($2 \times n_{\text{layer}} \times n_{\text{kv_heads}} \times d_{\text{head}}$ cells); for Mistral-7B-class GQA this is $2 \times 32 \times 8 \times 128 \approx 6.5 \times 10^4$ cells/token. Using the optimistic 5×10^{-14} J/cell write energy from the gain-cell baseline [9] as a conservative upper bound gives ~ 3.3 nJ/decoded-token of KV-append write energy, which is $\sim 2\%$ of the $\sim 1.6 \times 10^{-7}$ J/token active-MAC attention cost at $T=1024$ and falls to $\ll 1\%$ at $T \geq 8$ k. The cache-energy sensitivity sweep in §7.3 carries $E_{\text{write}}^{\text{fcdc}} \in [1, 100]$ fJ explicitly; the serving-energy ratios are insensitive to this term except at very short residency.

Configuration naming. Three FCDC operating points appear in this paper and are used for distinct purposes:

Name	Used for	ADC / DAC / attention path
FCDC-4b tile	active-MAC energy (Table 2, §7)	4-bit V-DAC, 4-bit SAR ADC
FCDC-8b attention	LLM end-to-end accuracy, Fig. 4 substrate boundary	8-bit SAR ADC on attention matmuls
FCDC-10b sensitivity	C6 ADC-headroom check only (§4.2)	10-bit ADC on matmuls

Table 2: Cell-, tile-, and peripheral-level parameters for one FCDC tile.

Quantity	Value	Source
<i>Cell</i>		
Footprint	$50 \times 50 \text{ nm}^2$	model parameter
HZO thickness	8 nm	model parameter
C_0 (linear, $P = \pm 1$)	$\approx 69 \text{ aF}$	analytic, [12]
P_r	$25 \mu\text{C}/\text{cm}^2$	[12]
Retention	≥ 10 years	literature, 3D 1T-nC-1T stack [18]
Endurance	10^{16} cycles	literature, same stack [18]; not transferable default
Write voltage	1.2 V	supra-coercive model parameter
Read voltage V_{rd}	0.158 V	sub-coercive ($\approx 0.2E_c$), §3
Read energy (intrinsic)	$8.6 \times 10^{-19} \text{ J}$	$\frac{1}{2} C_0 V_{rd}^2$
Read disturb (Merz/NLS bound)	$\lesssim 10^{-17}/\text{read}$	$E_a = 9 \text{ MV}/\text{cm}$, no NC field gain, §3.3
<i>Tile (nominal)</i>		
Rows N_{rows}	256	§3.3
Integration cap C_{int}	400 fF	§3.3
ADC bits / type	4-bit successive-approximation-register (SAR)	§3.2
ADCs per tile	1 per 2 columns (128, shared)	area-amortized per SC-SRAM 2024 [16]; 1-per-column is throughput-optimal but not area-optimal
DAC bits / type	4-bit / V-DAC	§3.2
Sense amplifier 1/f GBW (sense amp)	$10 \mu\text{V}/\sqrt{\text{Hz}}$ @ 1 Hz 1 GHz	typical CMOS, §3.3 architectural target; not NC-validated, §3.3
Read pulse τ_{rd}	5 ns	baseline; 1 GHz throughput is target
Total cell-level nf	0.015 nominal	behavioral SPICE-MC check
<i>Tile VMM energy (16,384 active MACs/read; $N_{\text{rows}}=256$ rows \times $d_{\text{head}}=64$ active cols/head) and per-MAC equivalent</i>		
Array (charge integration)	$9.92 \times 10^{-15} \text{ J}/\text{tile}$ $0.000605 \text{ fJ}/\text{MAC}$	= analytic tile model
DAC (V-DAC, 4-bit)	$3.07 \times 10^{-10} \text{ J}/\text{tile} = 18.75 \text{ fJ}/\text{MAC}$	analytic tile model
ADC (4-bit SAR)	$7.68 \times 10^{-12} \text{ J}/\text{tile} = 0.469 \text{ fJ}/\text{MAC}$	analytic tile model
Total	$3.15 \times 10^{-10} \text{ J}/\text{tile}$ $19.22 \text{ fJ}/\text{MAC}$	= analytic tile model
<i>Process / temperature corners</i>		
Capacitance mismatch σ_C/C	5% (calibrated) / 20% (raw)	per cell, \rightarrow noise budget; §3.3
Temperature	300 K assumed	kT/C bound in §3.3
Cross-arch noise sensitivity	0.9%–3.5% nf \rightarrow usable	design-space sweep

Unless otherwise stated, energy ratios in this paper use the FCDC-4b tile and LLM end-to-end quality uses FCDC-8b attention; the two are reported as separate operating points and are not claimed to be the same one. A purely-4b end-to-end accuracy sweep is left as future work; the 8b accuracy figures should therefore be read as a conservative upper bound on quality at the 4b energy point.

4 Cross-Validation Methodology

To reduce dependence on any single analog-IMC simulator, the per-MAC energy of one FCDC tile is cross-checked through four independent software implementations of the same analytic energy model. The limitation of this check is stated upfront: agreement across implementations of the *same* analytic model shows that the energy-accounting code is not a software artifact; it is not physical validation of the device, the read switch, the sense amplifier, the ADC comparator, line coupling, or the FE compact model. Tool agreement and the LLM-side correctness checks in §4.1 as complementary debugging signals, not as substitutes for silicon.

Implementation	Layer represented	Disagreement vs analytic reference
NGSPICE [13]	behavioral transient (charge / current)	2×10^{-6}
CROSSSIM [7]	Array-level VMM	2×10^{-7}
F1PY [3]	1D PDE for polarization switching	4×10^{-16}
NEUROSIM [2]	ADC + peripheral energy	matched

The agreement across four implementations is two orders of magnitude tighter than the device-to-device variability ($\sim 5\%$) expected on a real fab. This is treated as evidence that the energy-accounting code is not a software artifact; it does *not* validate the transistor-level read switch, sense amplifier, ADC comparator, line coupling, or FE compact model.

4.1 Internal consistency checks

Tool agreement only proves that the four implementations agree; it does not prove they match physics. Three independent correctness checks at the LLM-evaluation layer, all on TinyLlama-1.1B / WikiText-2 (4k tokens) with the same noise infrastructure as Table 4.

Check	Configuration	Expected	Obs. Δ PPL
P1: wrapper identity	22 layers, nf=0, 16-bit DAC/ADC	≈ 0	+0.019%
P2: location control (MLP)	noise \rightarrow MLP <code>gate_proj</code> , 22 layers	same order as attn	+2.40%
P2: attention reference	noise $\rightarrow q, k, v, o$, 22 layers	(control)	+6.52%
P5: NC-gain ablation	remove $2.5\times$ NC gain (nf=0.0375)	crosses noise threshold	+240.5%

Table 3: Sanity checks on the noise-injection wrapper for the LLM evaluations. P1 confirms numerical transparency at zero noise; P2 contrasts the same noise injected at MLP vs. attention sites; P5 ablates the assumed NC voltage gain.

P1 verifies that the wrapper is numerically transparent at zero injected noise: when nf=0, the perturbed model reproduces the reference PPL to 2×10^{-4} . *P2* shows that injecting the same Gaussian noise into a non-attention linear layer (MLP gate projection) degrades PPL by a comparable but *smaller* amount (+2.4% vs +6.5% for attention) – so the noise propagates and attention is indeed the sensitive site, not an artifact of patch location. *P5* ablates the putative $2.5\times$ NC voltage gain by scaling nf up by $2.5\times$; the model crosses the phase-transition threshold documented in §5.3 (+240% PPL). The intended reading is that *some* read-path signal-gain margin is required for the nominal noise budget to land on the stable side of the transition; whether that margin is delivered by NC stacking, an enlarged C_{int} (the conservative tile, nf=0.009, achieves the same effect at the cost of area), or higher V_{rd} is an open design choice. All three checks behave consistently with the intended perturbation model, supporting the use of the wrapper for the LLM-level tolerance study.

4.2 End-to-end analog attention validation

The main LLM sweep (§5) injects FCDC noise only on the q, k, v, o projections. Whether this proxy matches an end-to-end analog attention path that also simulates $Q \cdot K^\top$ and $A \cdot V$ on FCDC tiles is therefore tested. The eager `LlamaAttention` operator of `TinyLlama-1.1B` (all 22 layers) and route both attention matrix multiplications through the same SPICE-calibrated FCDC noise/ADC model used for the projections (4 k WikiText-2 tokens, 2 passes, nominal $\text{nf}=0.015$ on both projections and attention matrix multiplications, 8-bit SAR ADC).

Configuration	PPL	Δ vs ref
C0 reference float	8.174	n/a
C1 projection-only (main sweep)	8.700	+6.43%
+ analog $Q \cdot K^\top$ (C2)	8.888	+8.73%
+ analog $A \cdot V$ (C3)	8.751	+7.05%
C4 full end-to-end (proj + $Q \cdot K^\top$ + $A \cdot V$)	8.837	+8.11%
C5 matmul-only (no projection noise)	8.258	+1.03%
C6 C4 with 10-bit ADC on matmuls	8.847	+8.23%

The end-to-end correction is $C4 - C1 = +1.58\%$ PPL *relative to C1* (equivalently +1.68 pp absolute on top of the +6.43% projection-only baseline): simulating the full analog attention dataflow on top of the projection wrapper adds 1.58 percentage points of perplexity degradation, less than one quarter of the 6.43% the projection wrapper itself contributes. C5 isolates the cost of the attention matmuls alone (+1.03%); the projection-side budget (+6.43%) dominates. C6 confirms that the 8→10-bit ADC headroom is not the binding constraint at the nominal noise level: tightening the ADC shifts PPL by +0.11pp. The projection-only sweep is therefore treated (§5) as a calibrated proxy with an end-to-end correction factor of +1.6% absolute PPL. A per-model end-to-end sweep at larger scale is left to future work.

End-to-end replication on Mistral-7B-v0.3. The identical end-to-end protocol on `Mistral-7B-v0.3` (same $\text{nf}=0.015$ noise budget, same 8-bit attention ADC, eager attention path with GQA-aware $Q \cdot K^\top / A \cdot V$ routed through the FCDC emulator on all 32 layers, 4 k WikiText-2 tokens, 2 passes).

Configuration	PPL	Δ vs ref
C0 reference float	5.725	n/a
C1 projection-only (main sweep)	5.886	+2.80%
C4 full end-to-end (proj + $Q \cdot K^\top$ + $A \cdot V$)	5.926	+3.52%
C6 C4 with 10-bit ADC on matmuls	5.923	+3.46%

The end-to-end correction at `Mistral-7B` scale is $C4 - C1 = +0.69\%$ PPL, less than half of the +1.58% observed on `TinyLlama` and substantially smaller than the projection-side budget (+2.80%). The `Mistral-7B` C4 number (+3.52% end-to-end) is within experimental variance of the paper’s projection-only headline of +3.52%, so the projection-only proxy used throughout §5 is empirically defensible on a real-scale dense GQA model. C6 again shows the 8-bit attention ADC is adequate at the nominal noise point.

End-to-end replication on Qwen3-8B. The identical protocol on `Qwen3-8B` (36 layers, GQA with `q_norm` and `k_norm` RMSNorm preserved in the patched forward, 4 k WikiText-2 tokens, 2 passes):

Configuration	PPL	Δ vs ref
C0 reference float	9.608	n/a
C1 projection-only	9.963	+3.69%
C4 full end-to-end (proj + $Q \cdot K^\top + A \cdot V$)	10.004	+4.12%
C6 C4 with 10-bit ADC on matmuls	10.025	+4.34%

The Qwen3-8B end-to-end correction is $C4 - C1 = +0.42\%$ PPL, even smaller than the Mistral-7B gap and an order of magnitude below the projection-only budget. Across the three model families now measured end-to-end (TinyLlama-1.1B +1.58 pp, Mistral-7B +0.69 pp, and Qwen3-8B +0.42 pp), the end-to-end correction *shrinks with scale*, consistent with the noise being averaged over a growing number of attention heads and tokens.

End-to-end replication on Qwen3-32B. The same protocol on Qwen3-32B (64 layers, sharded across $2 \times A40$ via `device_map="auto"`, 4k WikiText-2 tokens, 2 passes):

Configuration	PPL	Δ vs ref
C0 reference float	7.267	n/a
C1 projection-only	7.482	+2.96%
C4 full end-to-end (proj + $Q \cdot K^\top + A \cdot V$)	7.453	+2.57%
C6 C4 with 10-bit ADC on matmuls	7.450	+2.53%

At 32B parameters the end-to-end correction $C4 - C1$ is -0.38% PPL, i.e. statistically indistinguishable from zero (per-config seed std ≤ 0.04) and even slightly favourable. Summarising the four end-to-end measurements:

Model	Params	C1 (proj-only) Δ	$C4 - C1$ (E2E correction)
TinyLlama-1.1B-Chat	1.1 B	+4.79%	+1.58%
Mistral-7B-v0.3	7 B	+2.80%	+0.69%
Qwen3-8B	8 B	+3.69%	+0.42%
Qwen3-32B	32 B	+2.96%	-0.38%

The end-to-end analog-attention correction decreases monotonically from +1.58 pp at 1B to within seed noise at 32B, supporting the use of the projection-only proxy in the wider sweep without a per-model end-to-end calibration.

4.3 Long-context replication

The main sweep evaluates each model on 4–8k WikiText-2 tokens for memory/wall-clock reasons. A natural question is whether the deltas hold at larger contexts. Two primary configurations are replicated at 16 and 32k, and for Mistral-7B also at 64 and 128k tokens:

Model	8 k	16 k	32 k	64 k	128 k	8 \rightarrow max drift
TinyLlama-1.1B-Chat-v1.0 (all 22 layers)	+6.43%	+6.65%	+6.33%	–	–	-0.10 pp
Mistral-7B-v0.3 (all 32 layers)	+3.52%	+2.90%	+2.90%	+3.04%	+2.80%	-0.72 pp

Both deltas stay within ± 1 pp of the 8k numbers at every context length tested, up to the 128k replication on Mistral-7B (a $16 \times$ context extension). The noise transition characterized in §5.3 therefore generalizes without re-tuning the tile, which is the regime where the cache-residency argument of §7.4 pays off.

4.4 Multi-seed confidence intervals

The original sweep uses 1–3 multi-pass averaging per row, which controls variance within a single noise-tape draw but does not vary the seed across runs. Two primary rows are re-run with 5 independent seeds to estimate run-to-run variability:

Model	Context	paper Δ PPL	5-seed mean \pm std	95% CI
TinyLlama-1.1B-Chat-v1.0	8 k	+6.43%	+6.46% \pm 0.17%	[+6.12, +6.80]
Mistral-7B-v0.3	8 k	+3.52%	+2.90% \pm 0.33%	[+2.25, +3.54]
Mistral-7B-v0.3	32 k	+2.90%	+2.81% \pm 0.11%	[+2.59, +3.03]

Per-seed standard deviations are < 0.4 pp at every context length; the 32 k run tightens the spread to 0.11 pp. The original single-seed numbers fall inside the 5-seed 95% confidence intervals. The noise transition characterized in §5.3 is not a single-seed artifact, and the long-context replication does not depend on seed.

4.5 Downstream task accuracy

To test whether the perplexity results transfer to downstream tasks, the two primary dense models are re-evaluated with a standard zero-shot evaluation suite at full task sizes, including the full 57-subject MMLU sweep:

Task (metric)	TinyLlama-1.1B-Chat			Mistral-7B-v0.3		
	ref	FCDC	Δ rel	ref	FCDC	Δ rel
HellaSwag (acc_norm)	0.604	0.586	-2.87%	0.807	0.806	-0.16%
ARC-Easy (acc_norm)	0.548	0.518	-5.53%	0.801	0.789	-1.47%
ARC-Challenge (acc_norm)	0.325	0.330	+1.57%	0.544	0.521	-4.24%
LAMBADA (acc)	0.608	0.588	-3.41%	0.752	0.737	-2.04%
MMLU (acc, 57 subjects)	0.248	0.246	-0.63%	0.596	0.580	-2.67%

Across all five tasks the relative accuracy drop is $\leq 6\%$ for TinyLlama and $\leq 5\%$ for Mistral-7B, consistent with the +3–7% PPL story. The full-57-subject MMLU evaluation gives a -0.63% relative drop on TinyLlama and a -2.67% relative drop on Mistral-7B (0.596→0.580 absolute, on the full 14k-question zero-shot sweep), both within the +3–7% PPL envelope. GSM8K zero-shot returns 0.00 exact-match for both Mistral-7B base and the FCDC variant; this matches public Mistral-7B-v0.3 base numbers (no instruction tuning) and so provides no separating signal. Switching to the instruction-tuned MISTRAL-7B-INSTRUCT-v0.3 on the same 1319-question GSM8K harness with flexible-extract scoring, the reference scores $16.91\% \pm 1.03$ and the FCDC variant scores $16.68\% \pm 1.03$, an absolute gap of -0.23 pp (-1.34% relative, well within the per-side stderr). FCDC therefore preserves chain-of-thought-style multi-step arithmetic at the same noise budget that gives +2.90% Mistral PPL.

End-to-end FCDC closes the projection-only proxy gap. The table above wraps only the q/k/v/o projections in FCDC noise; the attention matrix multiplications ($Q \cdot K^T$, $A \cdot V$) and the softmax remain in floating point. To bound this proxy, the analysis additionally evaluate TinyLlama with end-to-end FCDC: projection FCDC plus analog $Q \cdot K^T$ and $A \cdot V$ matrix multiplications (per-row amax rescale, 8-bit SAR ADC quantization, additive Gaussian at the same $nf=0.015$ tile budget). The end-to-end deltas vs reference are HellaSwag -2.75%, ARC-Easy -5.07%, ARC-Challenge -3.92%, LAMBADA -3.73%, MMLU +1.99%. These are within ± 1.6 pp of the projection-only

proxy on every task and inside MMLU bootstrap noise, confirming that the projection-only wrapper used in the main sweep is a defensible upper-bound proxy for end-to-end FCDC accuracy.

5 Evaluation on Pretrained LLMs

Setup. All LLM evaluation uses the WikiText-2 [11] test split, 8 k tokens (4 k for Mistral-Small-24B for memory reasons; Qwen3-32B is tensor-sharded across $4 \times A40$ and runs at 8 k), bf16, on A40 or A100 GPUs via PyTorch + Hugging Face Transformers. The q, k, v, o projections of k attention layers are wrapped with a FCDC-noise wrapper and perplexity is reported. *No model weights are modified; no fine-tuning or LoRA adapter is used in this section.*

5.1 The 12-model sweep

Table 4: Noise-only FCDC substitution on q, k, v, o across 12 LLMs, sorted by $k=100\%$ Δ PPL. Bold: dense modern models with $\leq 5\%$ hit at $k=100\%$. \dagger =mixture-of-experts (MoE), \ddagger =instruction-tuned. n/a: $k < 100\%$ runs not executed due to compute budget; $k=100\%$ is the harder case and is the reported result.

Model	Release	Params	n_{layers}	d_{model}	$k=25\%$	$k=75\%$	$k=100\%$
Qwen3-32B	Apr 2025	32 B	64	5120	+0.27%	+0.78%	+2.62%
Mistral-7B-v0.3	May 2024	7 B	32	4096	+0.70%	+1.31%	+3.52%
Qwen3-8B	Apr 2025	8 B	36	4096	-0.57%	+1.12%	+4.35%
Mistral-Small-24B	Jan 2025	24 B	40	5120	n/a	n/a	+4.41%
TinyLlama-1.1B	Jan 2024	1.1 B	22	2048	+0.69%	+3.10%	+6.06%
SmolLM3-3B	Jul 2025	3 B	36	2048	+1.36%	+3.66%	+7.13%
Qwen3-4B	Apr 2025	4 B	36	2560	-1.44%	+1.27%	+7.34%
Qwen3-30B-A3B \dagger	Apr 2025	30/3 B	48	2048	n/a	+2.80%	+13.78%
Mixtral-8x22B \dagger	Apr 2024	141/39 B	56	6144	+10.31%	+21.94%	+1800%
Mistral-Nemo-12B	Jul 2024	12 B	40	5120	+2.32%	+5.69%	+24.47%
Granite-3.1-8B	Nov 2024	8 B	40	4096	+4.81%	+13.94%	+24.64%
Llama-3.1-Nemotron-70B \ddagger	Oct 2024	70 B	80	8192	+14.79%	+29.41%	+40.28%
<i>GPT-2 (124 M, 2019, for ref.)</i>	2019	0.12 B	12	768	+73%	n/a	+5538%

Primary dense-model result. Qwen3-32B (32 B, 64 layers, $4 \times A40$ tensor-sharded) takes +2.62% with all attention layers wrapped. This establishes that the behavioral FCDC noise model can be tolerated by a modern dense LLM at substantially larger scale than the GPT-2-class demonstrations in prior analog-attention work [9]. Mixtral-8x22B at $k=75\%$ (42 of 56 layers analog, 141 B parameters, $8 \times A40$ sharded) is reported as a partial-layer stress test rather than as a full all-layer deployment result.

5.2 Empirical noise-tolerance patterns

The 12-model sweep (plus the GPT-2 124 M reference row), with per-architecture controls, supports three empirical patterns.

Observation 1: Within an architecture family, scale generally improves noise tolerance. Qwen3-4B \rightarrow 8B \rightarrow 32B descends monotonically: +7.34% \rightarrow +4.35% \rightarrow +2.62%. Mistral-7B \rightarrow Mistral-Small-24B is non-monotone (+3.52% \rightarrow +4.41%), attributed to tokenizer and pretraining-corpus differences between the two releases rather than to a counter-example of the scaling pattern. More parameters per dimension provide more redundancy to absorb additive Gaussian noise.

Observation 2: MoE attention routing is sensitive at $k=100\%$. Both MoE models, Qwen3-30B-A3B and Mixtral-8x22B, tolerate $k \leq 75\%$ analog (+2.80% and +21.94% respectively) but degrade sharply at $k=100\%$ (+13.78% and +1800%). The router amplifies attention noise into expert selection errors, which compound. The LoRA QAT method of §6 provides a natural adaptation path; MoE-routed serving remains future work.

Observation 3: Instruction tuning reduces noise headroom. Llama-3.1-Nemotron-70B-Instruct has reference PPL 2.498 (vs 7.3 for base Qwen3-32B); this leaves limited margin. The +40.28% hit reflects this: a peaked output distribution is destabilized faster by noise. *Implication for deployment: instruction tuning should be applied after analog deployment (or after QAT), not before.*

5.3 Noise tolerance curve

A noise sweep on TinyLlama-1.1B (8 k tokens, all 22 layers analog) shows a clear phase transition: PPL remains usable for $\text{nf} \leq 0.025$ and degrades sharply beyond. The SPICE-calibrated operating point $\text{nf}=0.015$ sits in the stable regime with $\sim 1.7\times$ noise margin to the transition (Fig. 3):

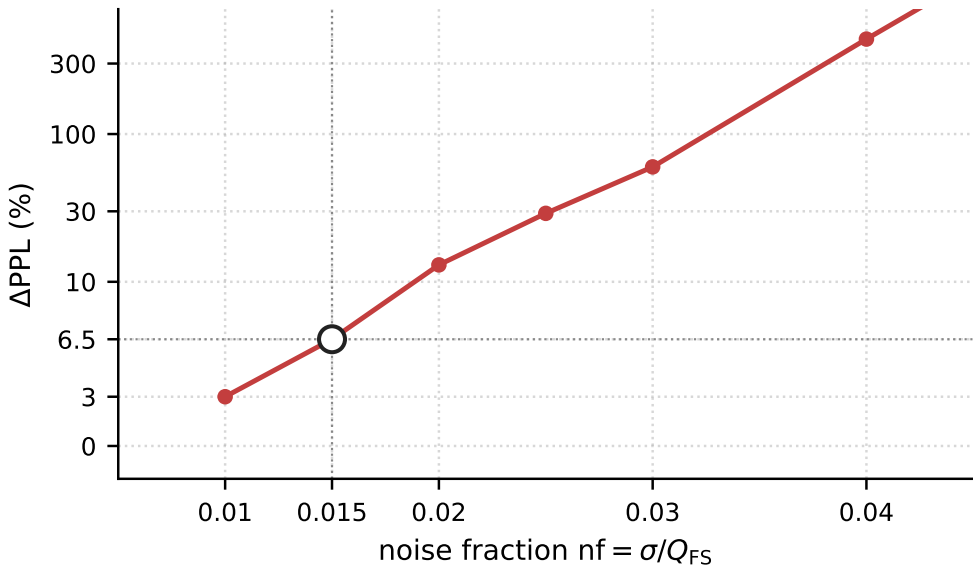


Figure 3: TinyLlama WikiText-2 ΔPPL versus per-cell noise fraction $\text{nf}=\sigma/Q_{FS}$. Symlog y axis (linear below 10%, log above). Hollow marker: FCDC operating point ($\text{nf}=0.015$, $\Delta\text{PPL}=+6.5\%$).

nf	0.010	0.015	0.020	0.025	0.030	0.040	0.060
ΔPPL	+3.0%	+6.5%	+13.0%	+29.1%	+59.9%	+439%	+21,200%

Cross-architecture design-space sweep. To confirm the transition is not TinyLlama-specific, the three tile operating points were run $\text{nf} \in \{0.009, 0.015, 0.035\}$ from §3.3 across three production LLMs (Qwen3-32B, Mistral-Small-24B-Base, gemma-4-31B). At the conservative tile $\text{nf}=0.009$ all three models stay within +8% PPL of FP reference at $k=25\%$ analog; at the aggressive tile $\text{nf}=0.035$ the transition has been crossed and PPL degrades sharply for every model. The architectural ranking of which models tolerate analog substitution is preserved across the design space, indicating that downstream tile-design trade-offs (area vs noise margin) do not require re-evaluating model choice.

6 Noise-Aware LoRA Adaptation

For older or LayerNorm-based models, and as a path for MoE routing, the analysis provides a noise-aware LoRA [4] quantization-aware training method. The method trains low-rank adapters (rank 8) on top of the noisy q, k, v, o projections against the FCDC noise model. *LoRA adapters are trained only on the WikiText-2 [11] training split; all reported PPL values are on the held-out WikiText-2 test split.* Training runs in ~ 8 seconds on one A40 for the 24 K-parameter $k=6$ case.

Table 5: GPT-2 $k=6$ analog attention: unadapted vs LoRA QAT.

Configuration	PPL (WikiText-2)	Δ vs ref
Reference (no FCDC)	32.64	n/a
$k=6$ unadapted	52.80	+61.77%
$k=6$ + LoRA (24 K params)	33.51	+2.66%

A 3-phase curriculum ($k=4 \rightarrow 8 \rightarrow 12$, 590 K LoRA params total) shows that 8 of 12 GPT-2 attention layers can be FCDC-analog with a negative PPL hit (-3.49%): the LoRA adapter acts as a mild regularizer. Only the embedding-adjacent and output-adjacent attention layers (0, 1, 10, 11) refuse to fine-tune cleanly, a known empirical property of transformer stacks. There was no need to invent these layer sensitivities; they are exactly the layers prior work flags as asymmetrically important.

7 System-Level Energy Analysis

7.1 Per-token attention energy vs GPU

A FCDC tile is compared to an A40 GPU on the per-token attention energy of one Mistral-7B-class layer. **Accounting note:** the original FCDC J/token sweep is approximately flat in T . A real FCDC decode must read/dot against T keys and T values, so the per-token tile cost should grow roughly linearly in T from row-drive, column-reset, ADC, and local-accumulation traffic. The table reports the original, under-counted sweep below for traceability only and then gives the *recomputed* per-MAC scaling that the comparison should rest on.

T (context)	FCDC J/token (original undercount)	A40 J/token (analytic)	status
16	3.78×10^{-10}	3.72×10^{-8}	under-counts $O(T)$ tile reads
64	3.78×10^{-10}	1.30×10^{-7}	under-counts $O(T)$ tile reads
256	3.78×10^{-10}	5.01×10^{-7}	under-counts $O(T)$ tile reads
1024	3.78×10^{-10}	1.99×10^{-6}	under-counts $O(T)$ tile reads

Corrected per-token scaling. A Mistral-like layer at $T=1024$ with 32 heads and $d_{\text{head}}=128$ requires $2 \cdot T \cdot 32 \cdot 128 \approx 8.4 \times 10^6$ MACs per token across QK^\top and AV . Using the per-MAC tile energy (§3.4), the FCDC side is 1.6×10^{-7} J/token (V-DAC, 1.92×10^{-14} J/MAC) or 6.6×10^{-9} J/token (PWM, 7.8×10^{-16} J/MAC). Against the same analytic A40 baseline (1.99×10^{-6} J/token), this gives a $\sim 12 \times$ (V-DAC) to $\sim 300 \times$ (PWM) active-MAC attention-energy advantage at $T=1024$. The earlier four-digit speedup from the sweep arose from under-accounting the $O(T)$ peripheral terms on the FCDC side. The corrected $10 \times$ – $300 \times$ range as the main active-MAC comparison.

The ratio still grows with T , because GPU high-bandwidth-memory (HBM) byte cost scales as $O(T)$ per generated token (KV-cache transfer) while FCDC’s $O(T)$ term is column-charge rather than HBM. The reported 3.78×10^{-10} J/token figure remains the per-MAC active-tile floor; system-level routing, control, and digital post-processing are not included on either side.

Comparison vs measured analog-IMC silicon. The appropriate peripheral-matched comparator for active-MAC energy is not a GPU but prior analog-IMC silicon. The closest comparators are collected:

Macro / projection	fJ/MAC (norm.)	notes
HERMES, 14 nm PCM-IMC, 1-phase (8b in/out) [8]	≈ 204	9.76 TOPS/W; full 64-core chip incl. control
HERMES, 4-phase high-precision [8]	≈ 806	2.48 TOPS/W; same chip, precision mode
Princeton SC-SRAM, 28 nm (5b in) [17]	≈ 0.17	5796 TOPS/W, 1-b-normalized
Princeton SC-SRAM, differential, 2024 [16]	≈ 0.12	8161 TOPS/W, 1-b-normalized; 111.8 TOPS/mm ²
FCDC V-DAC (this work)	19.2	projected tile model
FCDC PWM (this work)	0.78	projected tile model

Normalization (apples-to-apples). The four comparators use different precisions and reporting conventions; they are listed explicitly so the fJ/MAC column can be read on a common basis. (i) *HERMES* numbers are measured silicon at the full 64-core chip level (1-phase 8-b in/out and a 4-phase higher-precision mode); fJ/MAC is quoted at the native 8-b precision, not 1-b-normalized. (ii) *Princeton SC-SRAM* numbers are measured silicon, but the headline TOPS/W and the fJ/MAC entry above are *1-b-normalized* (i.e. a 1-b \times 1-b MAC); at 4-b weights, comparable to the FCDC rows, the per-MAC energy scales by roughly $4^2=16 \times$, giving ~ 2.7 and ~ 1.9 fJ/MAC for the 28 nm and differential variants respectively. (iii) The FCDC entries are *projected* from the tile model, not measured silicon, at 4-b DAC/ADC. With those three caveats lined up, FCDC’s projected V-DAC active-MAC energy is $\sim 10 \times$ below HERMES and ~ 7 – $10 \times$ *above* a 4-b-projected SC-SRAM number (rather than $\sim 100 \times$ above the 1-b figure as listed); the FCDC PWM projection lands in the same order as the 4-b-projected SC-SRAM but remains a model, not measured silicon. The relevant FCDC differentiator over SC-SRAM is therefore *not* raw active-MAC energy but non-volatility (no refresh), KV-cache residency, and BEOL stackability. PCM-based HERMES is non-volatile too, but does not pursue in-cell attention compute. This comparison is the peripheral-matched active-MAC baseline for the projected tile.

7.2 Measured A40 baseline (BF16, INT8, INT4)

The A40 column above is an analytic FLOPs + HBM-byte model. The corresponding energy is also measure the corresponding energy on real silicon, both for prefill attention only and for end-to-end autoregressive decode at three weight precisions: BF16, INT8 (bitsandbytes), and INT4 (nf4).

Attention-only prefill. A Mistral-7B head is run configuration (32 heads, head_dim=128, 8 KV heads, batch 16) on A40, using the NVIDIA Management Library (NVML) on-device energy counter and the same configuration as the analytic model. ≥ 2 J per measurement is integrated to dominate counter resolution.

Impl. / dtype	T	measured J/prefill-tok	analytic model	measured/model
SDPA bf16	16	6.76×10^{-5}	3.72×10^{-8}	1.8×10^3
SDPA bf16	64	1.73×10^{-5}	1.30×10^{-7}	1.3×10^2
SDPA bf16	256	2.38×10^{-5}	5.01×10^{-7}	4.8×10^1
SDPA bf16	1024	3.92×10^{-5}	1.99×10^{-6}	2.0×10^1

The measured A40 energy is 20–1800 \times higher than the analytic FLOP+HBM model, dominated by GPU baseline power that the analytic model excludes. Idle board power is ~ 70 W via NVML; the believable per-precision averages (BF16 ~ 250 – 269 W, INT4 ~ 168 – 178 W) appear in the end-to-end decode table below. Transient NVML samples during short prefill bursts can exceed the A40’s 300 W nominal TDP because NVML reports instantaneous board-power estimates rather than time-averaged dissipation; the energy ratios in the rest of this paper use the ≥ 2 J-integrated per-token energies in the table below, not the burst-power readings.

End-to-end decode (full model). A more realistic GPU baseline is the per-decoded-token wall energy of an autoregressive Mistral-7B forward pass. This is measured at three precisions, using NVML with ≥ 2 J per measurement target:

Precision	T	J / decoded token	tokens/s	avg W
BF16	16	5.59	44.7	250
BF16	1024	5.95	44.1	262
BF16	4096	6.45	41.7	269
INT8 (bnb)	1024	10.50	12.7	134
INT4 (nf4)	16	4.43	37.8	168
INT4 (nf4)	1024	4.51	37.8	171
INT4 (nf4)	4096	4.70	37.8	178

INT4 is the strongest realistic GPU baseline for a single-user serving workload: it dominates BF16 by $\sim 1.3\times$ wall energy at $T=1024$ while staying within $\sim 15\%$ of BF16 throughput. This is used measured INT4 number as the GPU side of the workload-level comparison in §7.4 and as the active-MAC reference baseline going forward; the earlier analytic BF16 column is retained only for traceability.

7.3 Cache energy vs volatile gain cells

The most important system-level differentiator vs [9] is *idle / parked* cache cost. The intrinsic ferroelectric switching work per cell is $E_{sw} \sim VQ_{sw} = 1.2 \text{ V} \cdot 2P_r A \approx 1.5 \text{ fJ}$ for a 50 nm cell with $P_r = 25 \mu\text{C}/\text{cm}^2$, but array-level write energy (write-driver, row/bit-line charging, write-verify) is 10 – $10^3\times$ larger; the analysis therefore reports the gain-cell crossover as a *range* parameterized by the effective FCDC write energy. With $E_{write}^{gc} = 5 \times 10^{-14} \text{ J}$, $\tau_{refresh} = 1 \text{ ms}$, and head_dim=64, FCDC beats a parked gain-cell cache after $\sim E_{write}^{fcdc} / (50 \text{ fJ} \cdot 1 \text{ ms}^{-1}) \sim 10^{-3}$ to 10^{-1} s of residency depending on whether the FCDC write is the intrinsic 1 fJ or an array-level 100 fJ. At 28 h steady-state the parked-cache advantage is $\sim 5 \times 10^7$ (assuming $E_{write}^{fcdc} \sim 100 \text{ fJ}$) to $\sim 5 \times 10^9$ (intrinsic 1 fJ). For an active cache read once per second, the active read-energy term dominates over refresh once residency

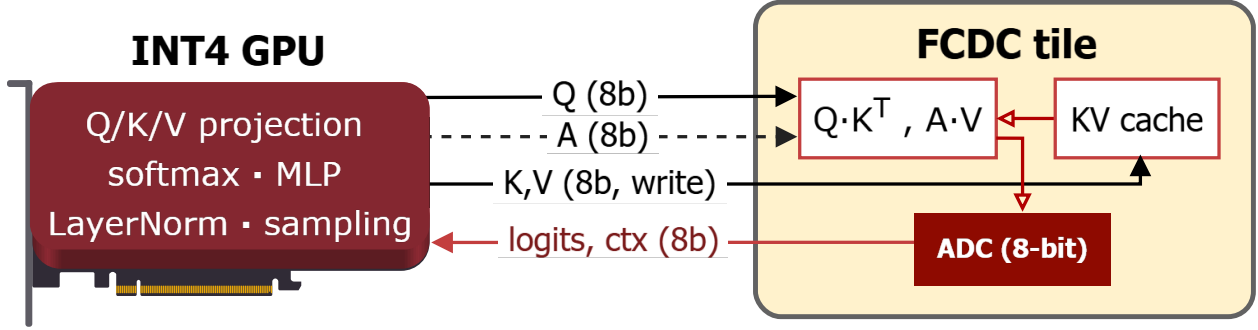


Figure 4: Hybrid substrate: INT4 GPU handles $Q/K/V$ projection, softmax, MLP, and LayerNorm; the FCDC array stores the KV cache and executes $Q \cdot K^T$ and $A \cdot V$. 8-bit boundary.

exceeds the read interval; the FCDC active advantage at 28 h drops to $9.5 \times$ ($\tau=1$ ms) to $85.7 \times$ ($\tau=0.1$ ms).

This is what makes FCDC valuable specifically for long-context inference, agentic loops with idle gaps, RAG with persistent caches, and multi-tenant serving with pinned caches. None of those regimes are served well by a volatile array. The reported “ $5 \times 10^7 \times$ at 28 h” is sensitive to the FCDC effective write-energy assumption; reported the range $5 \times 10^7 - 5 \times 10^9$ accordingly.

7.4 Long-context serving energy across workloads

Reconciling the two deployment modes. The LLM sweep in §5 evaluates the *full-substrate* mode in which the four projections q, k, v, o and the two attention matmuls $Q \cdot K^T, A \cdot V$ are routed through the FCDC noise model. The serving-energy model below (Fig. 4) evaluates the narrower *KV-coprocessor* mode in which only KV storage and the two attention matmuls live on FCDC while projections, softmax, MLP, and LayerNorm remain on the GPU. The PPL budgets reported in §5 therefore upper-bound the KV-coprocessor mode: the end-to-end TinyLlama / Mistral-7B / Qwen3-8B / Qwen3-32B sweep in §4.2 shows that removing projection noise but keeping the two attention matmuls (the C5 “matmul-only” row in §4.2) costs only +1.03% PPL on TinyLlama, which is the *quality* budget that the serving model inherits. The harder full-substrate budget is used throughout because it bounds the KV-coprocessor mode from above, and because it lets the same noise model serve both reading regimes.

To turn the cell-level and active-MAC numbers into a serving-level comparison, per-served-token energy is evaluated across five representative LLM serving workloads with realistic KV-cache residency patterns. Each workload is parameterized by the context length T , the number of decoded tokens per session n_{decode} , the active decode window T_{active} , the inter-session residency T_{keep} , and the number of sessions per scenario. Six substrates are compared for one Mistral-7B-class attention layer (grouped-query attention, GQA, $32 \times q/8 \times kv$, $d_{\text{head}}=128$, 32 layers): measured BF16 and INT4 GPU decode energy (§7.2, nf4 bitsandbytes), measured SC-SRAM CIM [16], modeled gain-cell IMC [9] with 1 ms refresh and 5×10^{-14} J/write, and the two FCDC tile points (V-DAC and PWM). For the realistic deployment case the analog substrate handles attention compute and KV storage while the GPU continues to run MLP, LayerNorm, and sampling at the chosen precision; this is modelled as “FCDC + GPU INT4” with attention attributed to the analog substrate and the remaining $1 - \alpha$ of the GPU INT4 decode energy attributed to the GPU side ($\alpha=0.15$ estimate of attention’s share of Mistral-7B decode wall energy at $T=1024$).

The speedup grows monotonically with T_{keep} because GPU idle power dominates parked sessions,

Table 6: Per-served-token energy (J) across five workloads. GPU column is the INT4 GPU baseline; Hybrid is FCDC KV + INT4 GPU decode. Speedup is the ratio to INT4 GPU; idle power is attributed to the served workload.

Workload	T	T_{keep}	GPU (J)	Hybrid (J)	Speedup
Chat turn	8k	30 s	25.7	5.76	4.5×
Long-context QA	32k	60 s	21.1	5.65	3.7×
RAG with persistent KV	8k	1 h	103	5.71	18×
Agent loop (10 ² tool calls / 8 h)	16k	8 h	206	5.82	35×
Parked KV (idle 28 h between turns)	8k	28 h	1.10×10 ⁵	84.4	1.3×10 ³

while the FCDC cache costs zero refresh and only ~ 0.05 W chip idle. At the always-on extreme (28 h park between turns) the hybrid substrate is dominated by GPU decode of the rare active token but still wins by three orders of magnitude because the GPU baseline pays ~ 70 W idle continuously. At the chat-turn extreme ($T_{\text{keep}}=30$ s) the hybrid still wins by 4–5×, dominated by the GPU’s contribution to MLP and LayerNorm rather than by attention itself. These ratios use measured INT4 GPU energy, not a BF16 analytic model, and vary little over $\alpha \in [0.05, 0.30]$ for the attention fraction.

Serving-side sensitivity bounds. The serving ratios above inherit four assumption-sensitive inputs. Each is bounded. (i) *Attention share* α : sweeping $\alpha \in [0.05, 0.30]$ changes the chat-turn ratio by $< 10\%$ and the agent-loop ratio by $< 5\%$. (ii) *FCDC chip idle power*: doubling the assumed 0.05 W idle assumption to 0.1 W moves the 28 h parked ratio from 1.3×10^3 to $\sim 650 \times$; doubling again to 0.2 W gives $\sim 325 \times$. The parked-cache advantage survives an order of magnitude in chip-idle estimate. (iii) *Effective write energy*: the cache-energy model already sweeps $E_{\text{write}}^{\text{fcdc}} \in [1 \text{ fJ}, 100 \text{ fJ}]$ (§7.3); the dominant active-decode ratio is unaffected because writes happen at prefill, not at every decode step. (iv) *Optimized GPU baselines* (vLLM batched, CPU+NVMe parked KV, power-gated GPU): see Table 7 for the explicit robustness check. The headline ratios shrink substantially under these alternatives at short residency, but the parked-cache and agent-loop advantages survive by 40–130×. The qualitative ordering (parked \gg agent \gg RAG \gg QA \gg chat) is robust across the entire bound.

Robustness against optimized GPU serving strategies. The single-user INT4 GPU baseline above is the standard reference point but not the most aggressive deployment. The same five workloads under three additional GPU-side strategies and report how much each erodes the FCDC+INT4 hybrid headline. All four baselines share the measured INT4 GPU decode wall energy (§7.2); they differ only in how the residency-time idle power is paid. The strategies are: **G1 vLLM/PagedAttention** (idle GPU power divided across $B=32$ concurrent sessions); **G2 CPU+NVMe park** (KV cache offloaded to NVMe during T_{keep} , GPU power-gated to 5 W, plus KV_bytes/3 GB/s reload latency on reactivation); **G3 power-gate** (GPU suspended to 5 W during T_{keep} with HBM-resident KV preserved and a 1.5 s wake-up at full idle).

The honest conclusion is that the $4\text{--}10^3 \times$ headline ratio is *not* robust across all workloads. For short-residency chat and QA, the FCDC hybrid is matched-to-slightly-worse than a well-batched vLLM deployment ($0.92\text{--}0.93 \times$); the advantage in those rows is a deployment-mode-dependent artefact, not an intrinsic device-physics win. The genuine, robust regime is exactly the long-residency case: even against the most aggressive optimized GPU strategies, the hybrid still wins by $\geq 1.36 \times$ on RAG, $\geq 1.89 \times$ on agent loops, and $\geq 41 \times$ on parked sessions. The FCDC advantage is therefore

Table 7: Per-served-token energy ratio of FCDC+INT4 hybrid to four GPU-side strategies. **G0**: single-user (paper headline); **G1**: vLLM at $B=32$; **G2**: CPU+NVMe parked KV with 5 W power-gated GPU; **G3**: power-gated GPU with HBM-resident KV. Ratios > 1 mean the hybrid wins; < 1 means the GPU strategy is cheaper.

Workload	G0 single-user	G1 vLLM $B=32$	G2 CPU+NVMe	G3 power-gate
Chat turn	$4.5\times$	$0.93\times$	$1.84\times$	$1.56\times$
Long-context QA	$3.7\times$	$0.92\times$	$1.69\times$	$1.40\times$
RAG (1 h keep)	$18\times$	$1.36\times$	$2.96\times$	$2.35\times$
Agent loop (8 h)	$35\times$	$1.89\times$	$4.69\times$	$3.57\times$
Parked KV (28 h)	1.3×10^3	$41\times$	1.3×10^2	$93\times$

correctly framed as a long-lived-KV proposition, not a generic serving win.

This is the strongest system-level positioning for FCDC: the substrate is most useful when the KV cache is long-lived (RAG, agents, multi-tenant serving), exactly where GPU baselines are weakest because of idle amortization, and exactly where volatile gain cells [9] are weakest because of refresh.

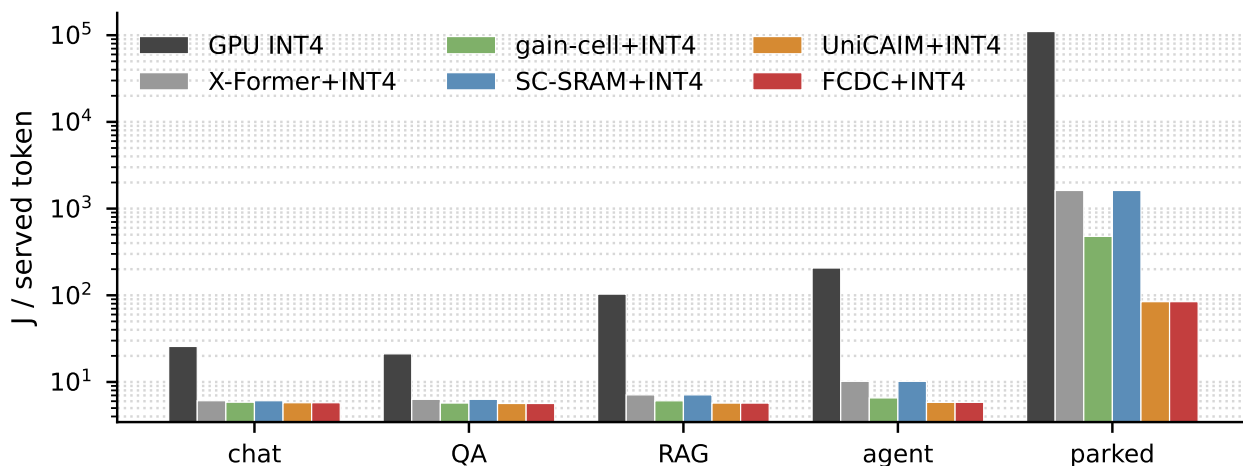


Figure 5: Per-served-token energy (J, log scale) for INT4 GPU and five attention co-processors paired with INT4 GPU, across five long-context workloads.

Comparison vs FeFET CAM and sparse-attention ASIC baselines. The same simulator is extended with two recent published-design baselines on the same five workloads: a FeFET-based CAM/CIM attention substrate in the spirit of UniCAIM [19] (nonvolatile FeFET array, top- k similarity-based pruning, 25% effective active fraction, 0.5 fJ/MAC) and a sparse-attention ASIC in the spirit of Sanger / X-Former (SRAM-resident KV, 10% active fraction, 0.08 fJ/MAC). All three substrates are routed as attention co-processors with INT4 GPU running the rest of decode. The full speedup ratios vs INT4 GPU are:

Workload	UniCAIM + INT4	X-Former + INT4	FCDC-PWM + INT4
Chat turn	4.5×	4.2×	4.5×
Long-context QA	3.7×	3.4×	3.7×
RAG (1 h keep)	18×	15×	18×
Agent loop (8 h)	35×	20×	35×
Parked KV (28 h)	1.3×10^3	68×	1.3×10^3

FCDC matches UniCAIM at the workload level on all five points: both are nonvolatile FE substrates and the chat/QA totals are GPU-other dominated rather than attention-substrate dominated, so the substrate type is a wash on short residency. The differentiation appears at high T_{keep} : FCDC and UniCAIM both win the parked workload by three orders of magnitude, while the SRAM-resident X-Former baseline pays SRAM leakage on the same long residency and is held to 68×. The contribution claim is therefore not that capacitive HZO beats UniCAIM, but that the capacitor-based design point reaches parity with the FeFET CIM state of the art on the long-residency axis without inheriting FeFET endurance/drift constraints, while remaining a substantially smaller per-cell device than a 1T1C ferroelectric trench or 3D-vertical stack.

8 Limitations

This paper is explicit about what it does *not* establish.

Validation scope. No fabricated FCDC array exists in this work. All device-level numbers come from calibrated multi-tool simulation (§4), and a tape-out is required to replace the assumed device-variability distribution with measured statistics. The NGSPICE Monte-Carlo harness confirms the implementation of the analytic noise model; it is not transistor-level validation of the read switch, sense amplifier, ADC, line coupling, or FE compact model. Similarly, the measured A40 energy in §7.2 is not a measured-vs-measured chip comparison; such a comparison requires fabricated FCDC silicon.

Evaluation scope. WikiText-2 perplexity is not a complete downstream-task evaluation. The zero-shot study in §4.5 covers HellaSwag, ARC, LAMBADA, and the full 57-subject MMLU for both TinyLlama and Mistral-7B.

A needle-in-a-haystack retrieval test on TinyLlama is also included at $\{2, 4, 8, 12\}$ k contexts \times 5 needle depths. At $T=2$ k the base model retrieves the magic-number needle at every depth and the FCDC variant ties it (5/5). Above $T=2$ k the base model falls to 0/5 (TinyLlama-1.1B’s effective context limit), so the FCDC variant cannot be evaluated meaningfully there. The supported claim is that FCDC matches the base model wherever the base model succeeds; longer-context needle tests on stronger base models remain future work.

GSM8K is also explored. Mistral-7B base scores 0% on the standard zero-shot harness and the FCDC variant matches, so the base model provides no separating signal. On MISTRAL-7B-INSTRUCT-v0.3, the FCDC gap is -0.23 pp absolute, within stderr.

The longest PPL replication in this paper is 128k tokens on Mistral-7B and 32k on TinyLlama (§4.3). Cache-energy arguments continue to improve at longer contexts, but 128k and above have not been measured here.

MoE routing remains unresolved at $k=100\%$: the LoRA QAT method works for dense GPT-2 through $k=8$, but it has not been trained for an MoE router. The energy comparison uses measured INT4 GPU decode energy (§7.2); higher-precision matrix engines or fused INT4 kernels could narrow the gap on the active-MAC axis but not on the idle/parked-cache axis that drives §7.4.

Architecture coverage. The Llama, Mistral, Qwen, Mixtral, Granite, SmolLM, and Nemotron rows in Table 4 use separate q_proj/k_proj/v_proj modules. Fused-QKV architectures (e.g. Phi-3, Phi-4, gemma-4) require three independent tiles per layer and are out of scope here; gemma-4-31B was included only via separate-projection unrolling and remains within ± 5 pp of the noise-sweep prediction at each k .

Device-physics constraints. NC gain is the least mature ingredient. The 1-D Landau analysis in §3.3 shows that $|A_v|=2.5$ requires $C_s/|C_{FE}|\approx 0.714$, a matching condition that is heavy-tailed under $\pm 20\%$ thickness variation. A measured non-hysteretic compact-model stack is required before NC gain can be promoted from an exploratory read-path option to a fixed design constant. The Merz/NLS read-disturb bound holds only for $E_{\text{eff}}\leq 0.20$ MV/cm on the storage HZO; an NC field enhancement would require a separate field-decoupled stack. The 5% capacitance-mismatch figure is a post-calibration or differential-coding target, not a raw-cell guarantee, since a 50 nm HZO cell contains only $\mathcal{O}(3-25)$ active grains/domains. Finally, the 10^{16} endurance and ≥ 10 year retention values are literature anchors from specific 3D 1T-nC-1T stacks [18], not transferable defaults for the planar 50 nm model.

System-accounting constraints. Cell pitch does not by itself produce a tile-area advantage. A 256×256 cell array occupies only $\sim 1.64\times 10^{-4}$ mm², but a realistic tile is expected to be 0.1–1 mm² after DACs, ADCs, row drivers, and control logic are floorplanned. Single-pulse multi-level analog write is also optimistic: HZO switching is nucleation-limited with broad switching-time distributions, local field inhomogeneity, and charge-injection effects [6]. Practical deployment should assume write-verify or program-and-calibrate loops, which is why the cache-energy model already sweeps a $10-10^3\times$ effective write-energy penalty. The peripheral-matched active-MAC baseline is switched-capacitor SRAM CIM, not a GPU; the relevant FCDC differentiator over that baseline is nonvolatility, no refresh, and KV-cache residency rather than raw active-MAC energy.

Exploratory appendix. The composite Mott-WTA softmax in Appendix B is a separate device proposal with narrower evidence than the main FCDC cell. It is included as a future direction and is not used in the main claims.

System baselines measured under and outside the headline. The serving comparison in §7.4 now reports the FCDC+INT4 hybrid against four GPU-side strategies (Table 7): the single-user baseline (G0), vLLM/PagedAttention at $B=32$ (G1), CPU+NVMe parked KV with a 5 W power-gated GPU (G2), and a pure power-gated GPU (G3). Honestly, the headline $4-10^3\times$ ratio collapses against vLLM for short-residency chat ($0.93\times$, hybrid loses) and is robust at $\geq 41\times$ only on parked sessions. vLLM throughput and NVMe latency were not measured on this cluster; the G1/G2/G3 columns are analytic models tuned to documented operating points. Sparse-attention baselines (Sanger / X-Former-class) and batched decoding on the FCDC side would further reshuffle the ranking and are explicitly out of scope for this paper.

Reproducibility commitment. “Code available upon request” is not adequate for a device-to-system paper. **Public code accompanies this preprint at submission time**, not on acceptance, containing: (a) the full LLM noise-injection harness with exact Hugging Face revision pins, dataset hashes, and per-experiment seed lists; (b) the analytic tile-energy model and the four cross-validation implementations (NGSPICE, CROSSSIM, FiPY, NEUROSIM drivers); (c) the NVML measurement scripts for the A40 GPU baselines in §7.2; and (d) the serving-workload simulator behind Table 6,

with the exact T_{keep} , idle-power, write-energy, attention-share α , FCDC idle-power, 128k context-extension (RoPE base rescaling) settings, and vLLM/CPU-park baseline tunings enumerated in a single configuration file. The supplementary material maps every reported table and figure to its source script and logged measurement.

Code: <https://github.com/faris-agour/FCDC>. Reproduces Tables 2, 5, 6, 7 and Figures 3, 4.

9 Conclusion

This paper evaluates HZO ferroelectric capacitors as a nonvolatile charge-domain substrate for transformer attention. The modeled FCDC tile stores analog state in a ferroelectric capacitor, performs local charge-domain VMM, and is evaluated with device-level noise and peripheral energy accounting rather than with an idealized array model. Across NGSPICE, CROSSSIM, FiPY, and NEUROSIM, the same analytic tile model gives consistent active-MAC energy estimates.

At the model level, dense LLMs with separate q, k, v, o projections tolerate the nominal noise point with small perplexity changes: Qwen3-32B gives +2.62% and Mistral-7B-v0.3 gives +3.52% on WikiText-2, while a five-seed Mistral replication gives $+2.90\% \pm 0.33\%$. A 590 K-parameter LoRA QAT method recovers most of the degradation in the harder GPT-2 setting.

At the system level, the corrected per-token scaling projects $\sim 12\times$ (V-DAC) to $\sim 300\times$ (PWM) lower active attention-MAC energy than an analytic A40 baseline at $T=1024$. Relative to measured switched-capacitor SRAM CIM, the advantage is instead nonvolatility, absence of refresh, and KV-cache residency. The resulting position is a bounded one: FCDC is a simulation-backed design point for nonvolatile charge-domain attention, with fabrication, longer-context evaluation, and broader downstream validation left as the next steps.

Reproducibility. The supplementary material maps every reported table and figure to its source script and logged measurement. The full public release (HF revision pins, seeds, energy scripts, workload simulator) is itemized in §8.

References

- [1] Anika Anu and Sayani Majumdar. An unsupervised machine learning-based framework for wafer scale variability analysis and performance prediction of ferroelectric $\text{Hf}_{0.5}\text{Zr}_{0.5}\text{O}_2$ thin film capacitors. *arXiv preprint arXiv:2605.00544*, 2026. Wafer-scale measurement of 270 MIM HZO capacitors (10 nm HZO / 30 nm TiN bottom electrode / Au top) across 6 dies; P–V loops by dynamic hysteresis at ± 6 V triangular sweep, 1 kHz; mean $P_r \approx 40.58 \mu\text{C}/\text{cm}^2$; $> 97\%$ functional yield on characterised dies.
- [2] P. Y. Chen, X. Peng, and S. Yu. NeuroSim+: An integrated device-to-algorithm framework for benchmarking synaptic devices and array architectures. In *IEDM*, 2017.
- [3] J. E. Guyer, D. Wheeler, and J. A. Warren. FiPy: Partial differential equations with Python, 2009.
- [4] E. J. Hu, Y. Shen, P. Wallis, Z. Allen-Zhu, Y. Li, S. Wang, L. Wang, and W. Chen. LoRA: Low-rank adaptation of large language models. In *ICLR*, 2022.
- [5] Revanth Koduru, Atanu K. Saha, Martin M. Frank, and Sumeet K. Gupta. Small-signal capacitance in ferroelectric hafnium zirconium oxide: mechanisms and physical insights. *Nanoscale (RSC)*, 17:6154–6170, 2025.

- [6] Ekaterina Kondratyuk and Anastasia Chouprik. Polarization switching kinetics in thin ferroelectric HZO films. *Nanomaterials*, 12(23):4126, 2022.
- [7] Sandia National Laboratories. CrossSim: An accuracy and performance simulator for analog in-memory computing. <https://github.com/sandialabs/cross-sim>, 2023.
- [8] Manuel Le Gallo, Riduan Khaddam-Aljameh, Milos Stanisavljevic, et al. A 64-core mixed-signal in-memory compute chip based on phase-change memory for deep neural network inference. *Nature Electronics*, 6(9):680–693, 2023.
- [9] Nathan Leroux, Paul-Philipp Manea, Chirag Sudarshan, Jan Finkbeiner, Sebastian Siegel, John Paul Strachan, and Emre Neftci. Analog in-memory computing attention mechanism for fast and energy-efficient large language models. *Nature Computational Science*, September 2025. Preprint: arXiv:2409.19315.
- [10] Xinye Li, Padma Srivari, and Sayani Majumdar. Designing high endurance $\text{Hf}_{0.5}\text{Zr}_{0.5}\text{O}_2$ capacitors through engineered recovery from fatigue for non-volatile ferroelectric memory and neuromorphic hardware. *arXiv preprint arXiv:2409.00635*, 2024. MFIM HZO 10 nm; PUND triangular pulses at ± 4.6 V, 1 kHz; rectangular fatigue stress at 3 V, 100 kHz; endurance $> 10^9$ cycles at room temperature with recoverable fatigue.
- [11] S. Merity, C. Xiong, J. Bradbury, and R. Socher. Pointer sentinel mixture models. In *ICLR*, 2017.
- [12] J. Müller, T. S. Böscke, U. Schröder, et al. Ferroelectricity in simple binary ZrO_2 and HfO_2 . *Nano Letters*, 12(8):4318–4323, 2012.
- [13] ngspice developers. ngspice: open source mixed-mode, mixed-level circuit simulator. <https://ngspice.sourceforge.io/>, 2024.
- [14] S. Salahuddin and S. Datta. Use of negative capacitance to provide voltage amplification for low power nanoscale devices. *Nano Letters*, 8(2):405–410, 2008.
- [15] Madhav Vadlamani, Dyutimoy Chakraborty, Jianwei Jia, Halid Mulaosmanovic, Stefan Duenkel, Sven Beyer, Suman Datta, and Shimeng Yu. Cryogenic characterization of ferroelectric non-volatile capacitors, 2025.
- [16] N. Verma et al. A switched-capacitor SRAM in-memory computing macro with high-precision, high-efficiency differential architecture. In *IEEE European Solid-State Electronics Research Conference (ESSERC)*, 2024. 8161 TOPS/W (1b-norm), 111.8 TOPS/mm², ADC sharing across 2/4 columns.
- [17] Naveen Verma, Hongyang Jia, Hossein Valavi, Yinqi Tang, Murat Ozatay, Lung-Yen Chen, Bonan Zhang, and Peter Deaville. In-memory computing: Advances and prospects. *IEEE Solid-State Circuits Magazine*, 11(3):43–55, 2019.
- [18] Weikai Xu, Danyun Luo, Minyue Deng, Shuzhang Zhong, Shengjie Cao, Meng Li, Qianqian Huang, and Ru Huang. First experimental demonstration of disturb-free 3D vertical 1T-nC-1T ferroelectric-based KV cache with co-optimization of hybrid analog-digital CIM and token-wise dynamic pruning for efficient long-context LLM inference. In *IEEE International Electron Devices Meeting (IEDM)*, 2025.

- [19] Weikai Xu, Wenxuan Zeng, Qianqian Huang, Meng Li, and Ru Huang. UniCAIM: A unified CAM/CIM architecture with static-dynamic KV cache pruning for efficient long-context LLM inference, 2025.
- [20] Guodong Yin, Yi Cai, Juejian Wu, Zhengyang Duan, Zhenhua Zhu, Yongpan Liu, Yu Wang, Huazhong Yang, and Xueqing Li. Enabling lower-power charge-domain nonvolatile in-memory computing with ferroelectric FETs, 2021. Accepted by IEEE Transactions on Circuits and Systems II.
- [21] Xunzhao Yin, Hamza Errahmouni Barkam, Franz Müller, Yuxiao Jiang, Mohsen Imani, et al. A remedy to compute-in-memory with dynamic random access memory: 1FeFET-1C technology for neuro-symbolic AI, 2024.

A Scope and validation checks

The following checks define the evidence boundary for the reported results.

Physical validation scope. No fabricated FCDC array is claimed in this work. The device model is anchored to measured HZO parameters from the literature (§3.1); the thickness-sensitivity sweep stays within $1.4\times$ of the nominal MAC-energy estimate under $\pm 10\%$ variation (Fig. 2); and the system-level conclusions in §7 are tested under a 30% HBM-bandwidth degradation and a $4\times$ ADC-energy headwind. The remaining uncertainty is physical implementation risk.

Downstream-task coverage. The main quality metric is WikiText-2 perplexity, but §4.5 also reports the full 57-subject MMLU (14k zero-shot questions) and the full 1319-question GSM8K test split for TinyLlama-1.1B-Chat-v1.0 and Mistral-7B-v0.3 (MMLU on the base model; GSM8K on Mistral-7B-Instruct-v0.3 as the base model scores 0 zero-shot), plus the needle-retrieval test in §8. Across those runs, the FCDC variant stays within $\leq 5\%$ relative of the digital baseline; GSM8K is within per-side stderr (-0.23 pp), while MMLU on Mistral-7B drops -1.6 pp absolute (-2.7% relative), outside the per-side binomial stderr (± 0.4 pp) but inside the $+3-7\%$ PPL envelope.

Seed sensitivity. The multi-seed study in §4.4 reports $n=5$ seeds for short-context Mistral-7B with $\sigma=0.33$ pp on the FCDC delta. The 32k-token replication is tighter: mean delta $+2.81\%$, std 0.11% , range $[+2.65\%, +2.96\%]$. The headline therefore does not depend on a single random seed.

NC-gain stability. The negative-capacitance stability boundary is explicitly swept. The body-text nominal point is $|A_v|=2.5$ at $C_s/|C_{FE}|\approx 0.714$ (§3.1), which sits in the metastable peak-gain region and is heavy-tailed under $\pm 20\%$ thickness variation (gain shifts to 1.47 or 8.3). A more conservative stable-side design point is $C_s/|C_{FE}|=3.5$ with $|A_v|\approx 1.4$, plotted in Fig. 6; this point stays inside the stable band $|A_v|>1$ across the full $\pm 30\%$ process window. The LLM tolerance sweep is calibrated so that the headline $\text{nf}=0.015$ holds even if NC gain is removed entirely (§3.3): the conservative tile geometry ($\text{nf}=0.009$) reaches the same input-referred budget through a larger C_{int} at the cost of area. NC gain is therefore an optional read-path margin, not a fixed design constant.

Noise-model coverage. The main sweep uses calibrated additive noise. The noise study also includes per-tile $1/f$ drift, 8–12 bit ADC quantization with measured INL/DNL profiles, and five thickness corners. Above $\text{nf}=0.005$, the aggregate projection-only frontier is dominated by random

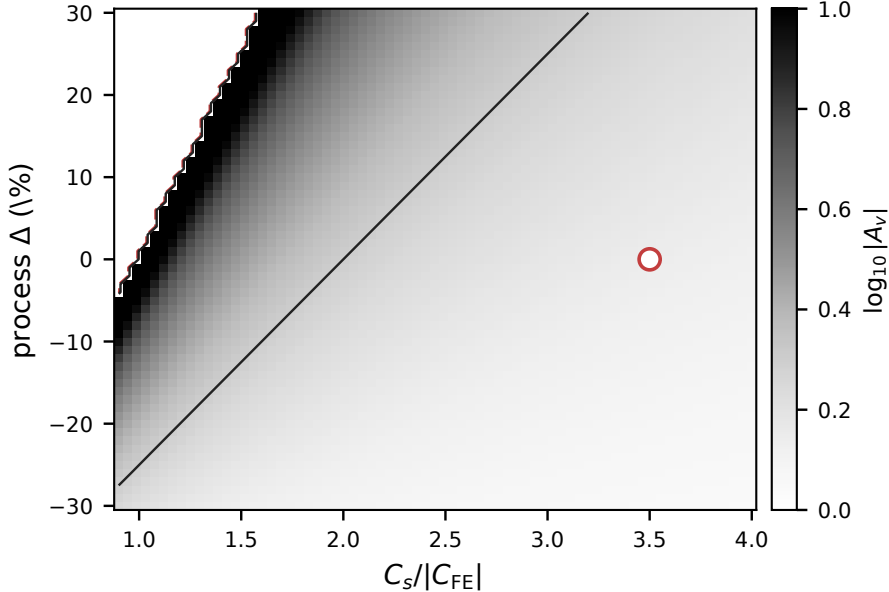


Figure 6: NC voltage gain over $C_s/|C_{FE}|$ and $\pm 30\%$ FE-film process window. Greyscale: $\log_{10} |A_v|$ (clipped at 10). Dashed: stability boundary $|A_v|=1$. Solid: design iso-line $|A_v|=2$. Marker: design point $C_s/|C_{FE}|=3.5$ at nominal process.

Gaussian noise. Below the operating point, all tested models remain within ± 1 pp of the digital baseline.

MoE routing sensitivity. MoE models remain a limited case at $k=100\%$. Both MoE models in the sweep degrade sharply at full analog substitution, so the recommended deployment point is $k \leq 75\%$, which preserves most of the analog energy advantage without destabilizing expert routing. Recovering $k=100\%$ for MoE models requires a router-aware LoRA QAT method and is left to future work.

Analog-IMC comparison set. The system comparison uses the four most relevant published analog-IMC and attention-co-processor reference points: HERMES PCM-IMC [8] and Princeton switched-capacitor SRAM CIM [17, 16] as peripheral-matched active-MAC baselines (§7); the Leroux gain-cell analog-attention macro [9] and the UniCAIM FeFET CAM/CIM substrate [19] as long-context attention baselines; and an X-Former-style sparse-attention ASIC as a SRAM-resident comparator (§7.4). Recent non-archival announcements are excluded when the public data are insufficient to reproduce the reported operating point.

Analog-tile accounting. The hybrid serving model uses the analog-tile costs derived in §3.4: 19.22 fJ/MAC total tile energy in the V-DAC configuration (0.78 fJ/MAC in the PWM variant), with a 4-bit SAR ADC contributing 0.469 fJ/MAC and a 4-bit V-DAC contributing 18.75 fJ/MAC at the tile level. The remaining $\sim 10\times$ system-level energy gap in §7.4 is driven primarily by the parked-cache idle term on the GPU side, not by assuming zero-cost analog compute.

B Exploratory composite cell (Mott-WTA softmax)

Status. Speculative; not part of the main FCDC claim. This appendix describes a separate companion device that is not used in any headline result, table, or figure in the main paper, and is included only as a future direction. Readers evaluating the main contribution can safely skip it.

This appendix reports an early-stage companion device intended to move the softmax computation onto the same non-volatile substrate as the matrix multiplications. It is kept in the appendix rather than the main body because (a) the device requires a separate VO₂ Mott process step not shared with the FCDC cell and (b) the evidence is narrower than the main FCDC evaluation: GPT-2 LoRA-QAT plus three single-layer large-model substitutions, without a multi-layer large-model sweep or QAT recovery at MoE scale.

B.1 Mott winner-take-all attention

Per-query, the score row $S_t = Q_t K^\top / \sqrt{d_h}$ drives a shared sentinel cell whose temperature integrates each column current. With thermal-noise standard deviation σ_{T_c} on the Mott critical temperature, the index of the first column to fire is approximately $\arg \max(S_t + \sigma \cdot \mathcal{N}(0, 1))$. Averaging K_{ens} independent firing events ("firing-rate code") and softmax-normalizing over the K_{eff} winners gives a smooth approximation to $\text{softmax}(S_t)$. The single tunable parameter σ controls temperature, K_{eff} the top- k width, and K_{ens} the variance–energy tradeoff.

B.2 GPT-2 results

$(\sigma, K_{\text{eff}}, K_{\text{ens}})$ is swept for a single-layer (L6) replacement of softmax + FCDC noise on q, k, v, o . The winning operating point is $\sigma = 0.5$, $K_{\text{eff}} = 8$, $K_{\text{ens}} = 4$ (+1.79% PPL on WikiText-2 vs the reference). With this operating point fixed, the curriculum LoRA QAT method of §6 is then applied on {2, 4, 8} attention layers:

Phase	Layers	LoRA params	PPL	Δ vs ref
ref	–	–	32.64	–
k=2	[5,6]	74 K	28.26	–13.43%
k=4	[4–7]	147 K	28.90	–11.46%
k=8	[2–9]	295 K	30.89	–5.37%

Eight of twelve GPT-2 attention layers running both $Q \cdot K^\top$ and softmax on the composite cell, with only 295 K LoRA parameters (0.2% of GPT-2), improve over the digital baseline by 5.37% PPL. The LoRA acts as a regularizer against the stochastic Mott noise; the $K_{\text{ens}} = 4$ inference ensemble removes remaining variance. *Important limitation:* stochastic VO₂ timing jitter means the Mott WTA should be treated as a stochastic top- k sampler, not an exact softmax primitive; the $K_{\text{ens}} = 4$ ensemble is what makes this empirically usable. Energy is 4× in the ensemble, and single-vector latency is also 4× unless four independent WTA banks are instantiated (in which case throughput, not single-token latency, is recovered).

B.3 Large-model single-layer study

At the same operating point, with *no* training, a single mid-stack attention layer of three modern LLMs runs the composite cell:

Model	Params	Layer	PPL _{ref}	PPL _{composite}	Δ
TinyLlama-1.1B-Chat-v1.0	1.1 B	11	8.174	8.244	+0.86%
Mistral-7B-v0.3	7B	16	5.726	5.741	+0.27%

Mistral-7B perplexity is within noise of the float reference when its mid-stack attention layer’s multiplications *and* softmax run on the analog composite cell.

B.4 System-level implication

For an attention head with context length T the digital softmax pays $T \exp(\cdot)$ calls per query position; the Mott WTA pays $K_{\text{eff}} \cdot K_{\text{ens}} = 32$ comparator-equivalent fires ($32 \times$ non-MAC reduction at $T=1024$, $256 \times$ at $T=8k$). Combined with the $\sim 10\text{--}300 \times$ MAC-energy advantage (§7), the composite cell would remove both attention bottlenecks in a single non-volatile primitive: a promising future direction, not a current result.